Inorg. Chem. **2008**, *47*, 6956−6963

Extended Triple-Bridged Ni(II)- and Co(II)-Hydroxamate Trinuclear Complexes: Synthesis, Crystal Structures, and Magnetic Properties

Z. Tomkowicz,[†] S. Ostrovsky,[‡] H. Müller-Bunz,[§] A. J. Hussein Eltmimi,[§] M. Rams,[†] D. A. Brown,[§] and W. Haase*,[||]

Institute of Physics, Jagiellonian University, Reymonta 4, 30-059 Kraków, Poland, Institute of Applied Physics, Academy of Sciences of Moldova, Academy str. 5, MD-2028 Chisinau, Moldova, Department of Chemistry, Centre for Synthesis and Chemical Biology, Convay Institute of Biomolecular and Biomedical Research, University College Dublin, Belfield, Dublin 4, Ireland, and Eduard-Zintl-Institute of Inorganic and Physical Chemistry, Darmstadt University of Technology, Petersenstrasse 20, 64287 Darmstadt, Germany

Received March 17, 2008

Crystal structures of new trinuclear complexes $[Ni_3(\mu\text{-}OAc_F)_4(\mu\text{-}AA)_2(tmen)_2]$, $[Ni_3(\mu\text{-}OAc_F)_4(\mu\text{-}BA)_2(tmen)_2]$, and $[Co_3(\mu\text{-}OAc_F)_4(\mu\text{-}BA)_2(tmen)_2]$ have been determined (OAc_F = CF_3COO^-, AA = acetohydroxamate anion, BA = benzohydroxamate anion, tmen = *N*,*N*,*N*′,*N*′-tetramethylethylenediamine). In each structure, the metal ions have distorted octahedral coordination and are triply bridged by one hydroxamate and two trifluoroacetate bridges. Magnetic properties of these compounds and of relative $[Co_3(\mu\text{-}OAc_F)_4(\mu\text{-}AA)_2(tmen)_2]$ were studied by susceptibility and magnetization measurements. It was shown that for nickel trimers the intramolecular magnetic coupling is weak ferromagnetic in the case of the complex with the AA group, and there is nearly no coupling in the case with BA group. Rather large zero field splitting was obtained for the distorted octahedral environments of the terminal nickel ions. The cobalt trimers were additionally studied by magnetic circular dichroism (MCD) measurements. The exchange interaction of the cobalt complexes is antiferromagnetic.

1. Introduction

Dinuclear metal hydrolases, which catalyze the hydrolysis of a range of peptide and phosphate ester bonds, contain a dinuclear metal site featuring Zn(II), Ni(II), Co(II), and Mn(II) with carboxylate bridges.[1] Hydroxamic acids are known inhibitors of the metallohydrolases[2] and feature a novel μ_2-η^1-η^2 hydroxamate with the deprotonated hydroxyl oxygen of the hydroxamate bridging the two metals of the dinuclear site and the carbonyl oxygen bonding one metal atom only as observed in the acetohydroxamate inhibited *Klebsiella aerogenes* urease and *Bacillus pasteurii* urease[3] and the model complex $[Ni_2(HShi)(H_2Shi)(pyr)_4(OAc)]$.[4]

The complexes $[M_2(\mu\text{-}O_2CR)_2(O_2CR)_2(\mu\text{-}H_2O)(tmen)_2]$ (M = Ni, Co, Mn; R = CH_3; tmen = *N*,*N*,*N*′,*N*′-tetramethylethylenediamine) consist of a dinuclear metal center with bridging carboxylates and a bridging water, making them ideal candidates for structurally modeling the dinuclear metallohydrolases. We have shown that hydroxamic acids react with a range of these dinuclear complexes to form μ_2-η^1-η^2 bridged hydroxamates with very similar structures to these shown by the inhibited ureases[3] and provide good biomimetic complexes. However, when R = CF_3, reaction of $[M_2(\mu\text{-}OAc_F)_2(OAc_F)_2(\mu\text{-}H_2O)(tmen)_2]$ (M = Co(II), Ni(II)) with aceto- and benzohydroxamic acids (AHA, BHA) gave the trinuclear complexes, $[M_3(\mu\text{-}OAc_F)_4(\mu\text{-}RA)_2(tmen)_2]$, M = Co(II), RA = AA (abbreviation **CoAA**); M = Co(II), RA = BA (abbr. **CoBA**); M = Ni(II), RA = AA (abbr. **NiAA**,

* To whom correspondence should be addressed. E-mail: haase@chemie.tu-darmstadt.de.
[†] Jagiellonian University.
[‡] Academy of Sciences of Moldova.
[§] University College Dublin.
[||] Darmstadt University of Technology.

(1) Wilcox, D. E. *Chem. Rev.* **1996**, *96*, 2435.
(2) Muri, E. M. F.; Nieto, M. J.; Sindelar, R. D.; Willliamson, J. S. *Curr. Med. Chem.* **2002**, *9*, 1631.
(3) (a) Pearson, M. A.; Nickel, L. O.; Hausinger, R. P.; Karplus, P. A. *Biochemistry* **1997**, *36*, 8164. (b) Ciurli, S.; Benini, S.; Rypniewski, W. R.; Wilson, K. S.; Miletti, S.; Mangani, S. *Coord. Chem. Rev.* **1999**, *331*, 190.
(4) Stemmler, A. J.; Kampf, J. W.; Kirk, M. L.; Pecoraro, V. L. *J. Am. Chem. Soc.* **1995**, *117*, 6368.

10.1021/ic800264y CCC: $40.75
Published on Web 07/02/2008

Table 1. Microanalytical Data for **NiAA, CoBA**, and **NiBA**

compound	abbr.		%C	%H	%N	%M
$[Ni_3(\mu\text{-}OAc_F)_4(\mu\text{-}AA)_2(tmen)_2] \times C_4H_{10}O$	**NiAA**	calcd	28.58	4.00	8.33	17.46
		found	29.14	4.06	8.07	16.89
$[Co_3(\mu\text{-}OAc_F)_4(\mu\text{-}BA)_2(tmen)_2]$	**CoBA**	calcd	36.03	3.91	7.41	15.60
		found	36.21	3.83	7.38	14.70
$[Ni_3(\mu\text{-}OAc_F)_4(\mu\text{-}BA)_2(tmen)_2]$	**NiBA**	calcd	36.05	3.92	7.42	15.54
		found	36.80	3.79	7.39	15.21

including solvent); M = Ni(II), RA = BA (abbr. **NiBA**) in which each hydroxamate bridges two metal centers in the μ_2-η^1-η^2 mode together with the doubly protonated salt $[(tmen)\cdot 2H][OAc_F]_2$.[5]

The structure of **CoAA** has been already described,[5] and in the present communication the structures of **CoBA**, **NiAA**, and **NiBA** are given together with the magnetic properties of all complexes, including **CoAA**.

Synthesis. Complexes **NiAA**, **NiBA, CoAA**, and **CoBA** were prepared similarly using appropriate reactants. The procedure for **CoBA** is as follows:

$[Co_2(\mu\text{-}OAc_F)_2(OAc_F)_2(\mu\text{-}H_2O)(tmen)_2]$ (0.5 mmol) was dissolved under nitrogen in methanol. A solution of 1 mmol of benzohydroxamic acid in methanol was then added and the mixture stirred for 1 hour. After filtration, the solvent was removed under vacuum to give a solid. Diethylether was added to the resulting solid, giving a white precipitate and a pink solution. The precipitate was dissolved in acetonitrile, and vapor diffusion of diethylether into the solution led to colorless needles of $[tmen\cdot 2H][OAc_F]_2$, suitable for X-ray crystallography. Yield: 0.26 mmol, 26%.

Pink crystals of $[Co_3(\mu\text{-}OAc_F)_4(\mu\text{-}BA)_2(tmen)_2]$, **CoBA**, suitable for crystallography formed from the above pink filtrate on standing at room temperature. Yield: 0.22 mmol, 66%. (microanalytical data, Table 1)

2. Experimental Section

Crystal data were collected using a Bruker SMART APEX CCD area detector diffractometer. A full sphere of reciprocal space was scanned by phi-omega scans. Pseudoempirical absorption correction based on redundant reflections was performed by the program *SADABS*.[6] The structures were solved by direct methods using *SHELXS-97*[7] and refined by full matrix least-squares on F^2 for all data using *SHELXL-97*.[8] Hydrogen atoms attached to nitrogen were located in the difference Fourier map and allowed to refine freely. All other hydrogen atoms were added at calculated positions and refined using a riding model. Their isotropic temperature factors were fixed to 1.2 times (1.5 times for methyl groups) the equivalent isotropic displacement parameters of the parent carbon atom. Anisotropic thermal displacement parameters were used for all non-hydrogen atoms.

DC magnetization measurements for polycrystalline samples were done with a Quantum Design SQUID magnetometer, model MPMS 5XL. The samples were pressed into pellets to avoid reorientation of grains in magnetic field. All temperature dependencies were measured in a magnetic field of 1000 Oe. Magnetization curves M(H) were measured up to $H = 50$ kOe at the constant temperature of 2 K. The data were corrected for the diamagnetism of the sample holder and for the core diamagnetic contribution.

MCD spectra were measured for cobalt complexes using a JASCO J-810 spectropolarimeter, interfaced with an Oxford Instruments cryostat Spectromag SM 4000−9T equipped with a split-coil superconducting magnet. The samples, thoroughly milled, were mixed with Nujol and placed between two thin quartz plates in a copper sample holder that was screwed to the lower end of the sample probe. The temperature was regulated by adjusting the helium gas flow rate from the main bath through the heat exchanger and by using two pairs of heater and thermometer mounted at the heat exchanger and at the sample probe near the sample. The accuracy of the temperature control was better than 0.3 K. The cryostat windows and the sample holder were checked to make sure that they were not giving MCD signals. Data acquisition was achieved using JASCO spectra manager software. The obtained MCD spectra were corrected by subtracting the small zero-field MCD signal.

3. Crystal and Molecular Structures

The general crystallographic data are given in Table 2. **NiAA** crystallizes in the orthorhombic space group *Aba*2 (No. 41) (this complex crystallizes with solvent $C_4H_{10}O$; we preserve the abbreviation **NiAA** for the full composition), whereas **NiBA** and **CoBA** crystallize in the monoclinic group $P2_1/n$ (No. 14). The nickel complexes show no internal symmetry, whereas in **CoBA**, as in the earlier published[5] **CoAA**(triclinic, $P\bar{1}$, No. 2), the central cobalt atom occupies an inversion center. Molecular structures of **NiAA**, **NiBA**, and **CoBA** are shown in Figures 1, 2, and 3, respectively. In all complexes, including **CoAA**, the environments of all three metal ions have distorted octahedral geometry, for example, for **NiAA** the angle O(1)−Ni(2)−O(6) is 91.0° and O(3)−Ni(3)−O(10) is 91.2°. The coordination of the central metal atom is O_6, and coordination of terminal metal atoms is N_2O_4. The main difference between the cobalt and the nickel complexes is the relative orientation of the bridging ligands: in the cobalt complexes, the hydroxamate groups are on exactly opposite sides of the Co−Co−Co line due to the inversion center, but in the nickel complexes the angle between them (given as the angle between the two average planes through the hydroxamate groups) are only 50° (**NiBA**) and 47° (**NiAA**).

The metal ions in **CoAA** and **NiAA** are triply bridged by a single acetohydroxamate bridge and two trifluoroacetates. Benzohydroxamate bridges instead of acetohydroxamate bridges are present in **CoBA** and **NiBA**. All structures are additionally stabilized by the intramolecular hydrogen bonding as shown in figures by the dashed line.

The bonding M−O−M angles in **NiBA** are the same and equal to 117.2°, but they are different in **NiAA**: the angle Ni2−O1−Ni1 is equal 116.7° and angle Ni1−O3−Ni3 is equal 118.1°. The M−O−M angles in **CoAA** are equal to 119.3° and in **CoBA** equal to 118.5°. The M−M−M angle in **NiAA** is 167.5° and 167.9° in **NiBA** and 180° in cobalt complexes.

(5) Brown, D. A.; Clarkson, G. J.; Fitzpatrick, N. J.; Glass, W. K.; Hussein, A. J.; Kemp, T. J.; Müller-Bunz, H. *Inorg. Chem. Commun.* **2004**, *7*, 495.
(6) Sheldrick, G. M. *SADABS*; Bruker AXS Inc.: Madison, WI, 2000.
(7) Sheldrick, G. M. *SHELXS-97*; University of Göttingen: Göttingen, Germany, 1997.
(8) Sheldrick, G. M. *SHELXL-97−2*; University of Göttingen: Göttingen, Germany, 1997.

Table 2. Crystallographic Data for **CoBA**, **NiAA**, and **NiBA**

identification code	**CoBA**	**NiAA**	**NiBA**
molecular formula	$C_{34}H_{44}N_6O_{12}F_{12}Co_3$	$(C_{24}H_{40}N_6O_{12}F_{12}Ni_3)_2 \times C_4H_{10}O$	$C_{34}H_{44}N_6O_{12}F_{12}Ni_3$
fw	1133.54	2091.62	1132.88
cryst syst	monoclinic	orthorhombic	monoclinic
space group	$P2_1/n$ (No. 14)	$Aba2$ (No. 41)	$P2_1/n$ (No. 14)
a	12.822(4) Å	16.0444(15) Å	12.340(2) Å
b	12.952(4) Å	36.222(3) Å	30.197(5) Å
c	14.699(4) Å	15.2264(14) Å	12.986(2) Å
α	90°	90°	90°
β	105.954(4)°	90°	92.645(3)°
γ	90°	90°	90°
V	2346.9(12) Å^3	8848.9(14) Å^3	4834.2(14) Å^3
Z	2	4	4
D_{calcd}	1.604 g/cm^3	1.570 g/cm^3	1.557 g/cm^3
absorption coefficient	1.157 mm^{-1}	1.372 mm^{-1}	1.262 mm^{-1}
F(000)	1150	4280	2312
cryst size	0.81 × 0.76 × 0.64 mm^3	0.50 × 0.40 × 0.40 mm^3	0.80 × 0.50 × 0.20 mm^3
h k l ranges	−16, 16, −16, 16, −18, 18	−20, 20, −46, 47, −19, 19	−14, 14, −29, 34, −14, 13
Reflections collected	37 872	36 970	21 973
independent reflns	5112 [R(int) = 0.0168]	10 223 [R(int) = 0.0240]	7489 [R(int) = 0.0239]
absorption correction	semiempirical from equivalents	semiempirical from equivalents	semiempirical from equivalents
max. and min. transmission	0.5247 and 0.4139	0.6098 and 0.5470	0.7864 and 0.6184
GOF on F^2	1.019	1.010	1.020
final R indices [$I > 2\sigma(I)$]	R1 = 0.0393, wR2 = 0.1080	R1 = 0.0402, wR2 = 0.0946	R1 = 0.0472, wR2 = 0.1160
R indices (all data)	R1 = 0.0424, wR2 = 0.1113	R1 = 0.0522, wR2 = 0.1014	R1 = 0.0578, wR2 = 0.1232
largest diff. peak and hole	0.897 and −0.467 e·Å^{-3}	0.647 and −0.266 e·Å^{-3}	0.625 and −0.369 e·Å^{-3}

The shortest M−M distances are 3.48 Å in both nickel complexes and 3.55 Å in cobalt complexes. Metal−ligand interatomic distances are given in Table 3.

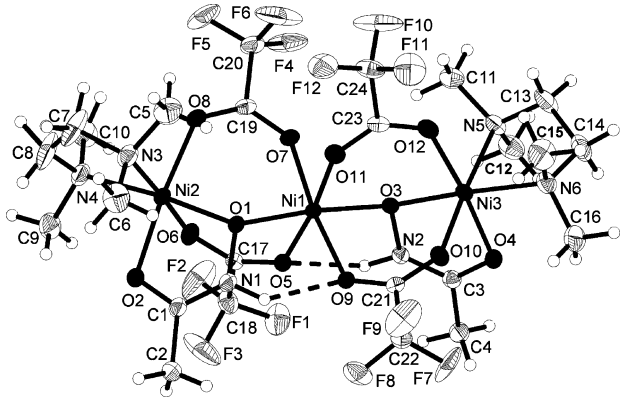

Figure 1. Molecular structure of $[Ni_3(\mu\text{-}OAc_F)_4(\mu\text{-}AA)_2(tmen)_2]$, **NiAA**. Thermal ellipsoids are drawn on the 15% probability level; disorder neglected for clarity. The solvent molecule is not shown.

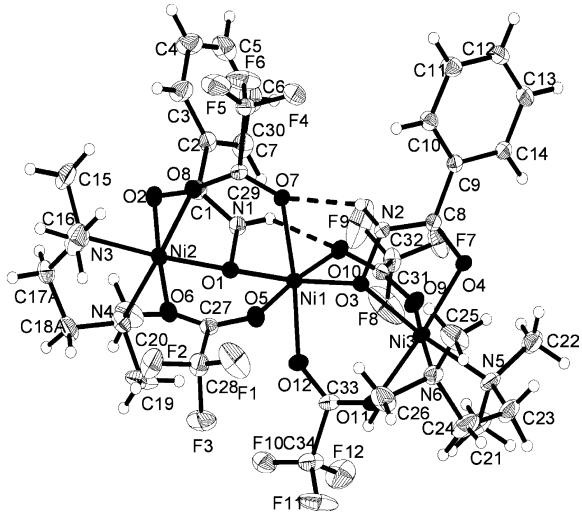

Figure 2. Molecular structure of $[Ni_3(\mu\text{-}OAc_F)_4(\mu\text{-}BA)_2(tmen)_2]$, **NiBA**. Thermal ellipsoids are drawn on the 50% probability level; disorder neglected for clarity.

4. Magnetic properties

4.1. Nickel Trimers. Temperature dependence of the χT product (χ-magnetic susceptibility) is shown in Figure 4 and magnetization M vs magnetic field H dependence (at $T = 2$ K) is shown in Figure 5 for both studied nickel compounds. From first glance at the figures, it seems that the nickel trimer in **NiAA** is internally ferromagnetically coupled, whereas the coupling in **NiBA** is antiferromagnetic. The data analysis will show that it is not obvious in the case of **NiBA**.

The ground state of the d^8 ion in an octahedral crystal field is an orbital singlet $^3A_{2g}$. Further splitting of spin levels is possible in the field of lower symmetry. It is so-called zero field splitting (ZFS). The detailed analysis of interactions for the nickel trimer was carried out using the following spin Hamiltonian:

$$\hat{H} = -2J_{ex}(\hat{S}_2 \cdot \hat{S}_1 + \hat{S}_1 \cdot \hat{S}_3) + \sum_{i=1}^{i=3} \hat{S}_i \cdot \hat{D}_i \cdot \hat{S}_i + \mu_B H \cdot \sum_{i=1}^{i=3} \hat{g}_i \cdot \hat{S}_i \quad (1)$$

The first term represents the isotropic magnetic exchange between the nearest neighbor Ni(II) ions. The second term represents ZFS. The last term in eq 1 is the Zeeman interaction. It consists of spin contribution only, with a S_i value equal to 1; μ_B is the Bohr magneton. Zero field splitting $\hat{D}_i$ and spectroscopic $\hat{g}_i$ tensors, expressed in their local principal axes coordinate systems, have the following diagonal forms,

$$\hat{D}_i^{loc} = \begin{bmatrix} -1/3D_i + E_i & 0 & 0 \\ 0 & -1/3D_i - E_i & 0 \\ 0 & 0 & 2/3D_i \end{bmatrix},$$

$$\hat{g}_i^{loc} = \begin{bmatrix} g_{i\perp} & 0 & 0 \\ 0 & g_{i\perp} & 0 \\ 0 & 0 & g_{\parallel} \end{bmatrix} \quad (2)$$

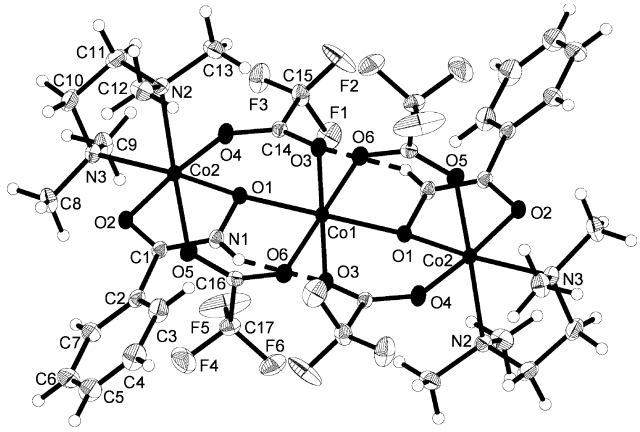

Figure 3. Crystal structure of $[Co_3(\mu\text{-}OAc_F)_4(\mu\text{-}BA)_2(tmen)_2]$, **CoBA.** Thermal ellipsoids are drawn on the 15% probability level; disorder neglected for clarity.

where D_i are the axial and E_i rhombic ZFS parameters. It was assumed that the principal axes of $\hat{D}_i^{loc}$ and $\hat{g}_i^{loc}$ tensors coincide.

Hamiltonian (eq 1) is written in the common molecular system. Using orthogonal transformation matrices ν_i, the $\hat{D}_i$ and $\hat{g}_i$ tensors in Hamiltonian (eq 1) can be expressed by the local tensors and Hamiltonian (eq 1) is transformed to the form

$$\hat{H} = -2J_{ex}(\hat{S}_2 \cdot \hat{S}_1 + \hat{S}_1 \cdot \hat{S}_3) + \sum_{i=1}^{i=3} \hat{S}_i \cdot \nu_i^{-1} \hat{D}_i^{loc} \nu_i \cdot \hat{S}_i + \mu_B H \cdot \sum_{i=1}^{i=3} \nu_i^{-1} \hat{g}_i^{loc} \nu_i \cdot \hat{S}_i \quad (3)$$

It is not easy to predict the directions of principal axes of the local tensors when the coordination octahedrons are distorted. We used the point charge model to find the principal axes by the diagonalization of the crystal electric field gradient tensors calculated at the nickel sites. The matrices build from the eigenvectors of the crystal field gradient tensors are our transformation matrices ν_i. These matrices were calculated for the various relations of the nitrogen to oxygen charge (in the limits from 1 to 0.75). For calculation details of ν_i matrices, see the Supporting Information.

The parameters J_{ex}, D_i, E_i, g_i were obtained from simultaneous fits of susceptibility vs T and magnetization vs H data. Such procedure allows determination of the sign of the D parameter from the powder data.[9] The full-matrix numerical diagonalization of the Hamiltonian was performed by a computer program. The calculated data of χ and M were averaged over many orientations.

The ferromagnetic coupling for **NiAA** can be relatively easily and unambiguously confirmed by fitting. Because anisotropy of g_i did not affect the fits, only the average value of g_i was retained. The large number of solutions was found with the **NiBA** data and they were of the worse quality than that for **NiAA**. They differed, first off all, with values and signs of D parameters; the absolute values of D were large. For that reason, we would like to check in detail the difference in geometry of the coordination polyhedrons of **NiBA** and **NiAA**. It was believed that, in this way, at least the signs of D can be predicted. We used again the point charge model and calculated the components of the crystal field gradient tensor to estimate the axial and rhombic distortion. This time, eigenvalues were considered. The results, expressed in the form of δ and ϵ parameters, are given in Table 4. The inequality $\delta < 0$, obtained for the central ion, is equivalent to the elongation of its O_6 octahedron. The axial distortion for the terminal nickel ions is of the opposite sign and a little greater than that of the

(9) Boča, R.; Dlhan, L.; Haase, W.; Herchel, R.; Maslejova, A.; Papankova, B. *Chem. Phys. Lett.* **2003**, *373*, 402.

Table 3. Metal-Ligand Interatomic Distances (Angstroms) in **NiAA**, **NiBA**, and **CoBA**

NiAA	NiBA	CoBA
Ni1−O1 2.049	Ni1−O1 2.052	Co1−O1 2.054
Ni1−O3 2.045	Ni1−O3 2.044	Co1−O3 2.155
Ni1−O5 2.069	Ni1−O5 2.040	Co1−O6 2.101
Ni1−O7 2.047	Ni1−O7 2.070	
Ni1−O9 2.06	Ni1−O10 2.084	
Ni1−O11 2.051	Ni1−O12 2.049	
Ni2−O1 2.037	Ni2−O1 2.027	Co2−O1 2.086
Ni2−O2 2.043	Ni2−O2 2.042	Co2−O2 2.093
Ni2−O6 2.128	Ni2−O6 2.041	Co2−O4 2.096
Ni2−O8 2.040	Ni2−O8 2.127	Co2−O5 2.096
Ni2−N3 2.147	Ni2−N3 2.135	Co2−N2 2.185
Ni2−N4 2.130	Ni2−N4 2.131	Co2−N3 2.191
Ni3−O3 2.023	Ni3−O3 2.043	
Ni3−O4 2.054	Ni3−O4 2.038	
Ni3−O10 2.111	Ni3−O9 2.109	
Ni3−O12 2.027	Ni3−O11 2.054	
Ni3−N5 2.162	Ni3−N5 2.139	
Ni3−N6 2.133	Ni3−N6 2.133	

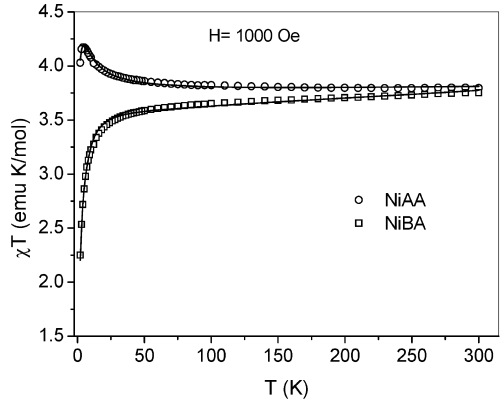

Figure 4. Temperature dependence of the χT product for two nickel complexes. Solid lines are fits (text for details).

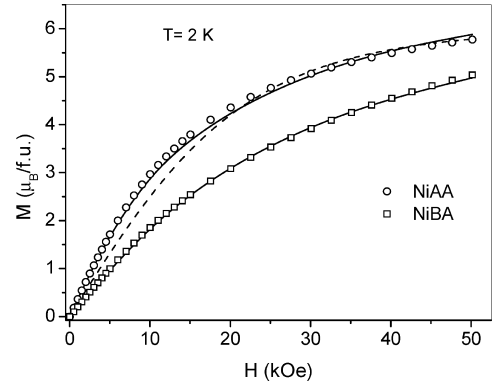

Figure 5. Magnetization M vs H curves for two nickel complexes. Solid lines are fits (text for details). The dashed line is the Brillouin curve for three free nickel spins calculated with $g = 2$.

Table 4. Electric Field Gradient Components at the Nickel Sites, Calculated in Their Local Principal Axes Systems, Using a Point Charge Model for **NiAA** and **NiBA**[a]

NiAA	Ni2	Ni1	Ni3
		$q_N/q_O = 1$	
δ_i	0.13	−0.09	0.12
ϵ_i	0.01	−0.02	0.02
		$q_N/q_O = 0.8$	
δ_i	0.17	−0.09	0.16
ϵ_i	0.02	−0.02	0.02
NiBA	Ni2	Ni1	Ni3
		$q_N/q_O = 1$	
δ_i	0.14	−0.10	0.11
ϵ_i	0.01	−0.02	0.01
		$q_N/q_O = 0.8$	
δ_i	0.17	−0.10	0.15
ϵ_i	0.02	−0.02	0.01

[a] δ_i is a measure of the axial distortion, and ϵ_i is a measure of the rhombic distortion (in arbitrary units).

Table 5. Best Fit Parameters for Nickel Trimers Obtained from Magnetic Data[a]

	NiAA	**NiBA**
J_{ex}(cm^{-1})	0.56 ± 0.05	∼0 ± 0.05
g_1	2.25 ± 0.04	2.19 ± 0.03
$g_2 = g_3$	2.23 ± 0.03	2.18 ± 0.03
D_1 (cm^{-1})	4.3 ± 0.5	3.9 ± 0.6
$D_2 = D_3$ (cm^{-1})	−7.0 ± 0.6	−13.9 ± 1.5
TIP (emu/mol)[b]	(188 ± 30) × 10^{-6}	(697 ± 60) × 10^{-6}

[a] Uncertainties reflect the influence of the starting parameters and of the way of the minimization on the final results. [b] TIP stands for temperature-independent paramagnetism

central nickel atom, assuming the same charge of all neighboring ions. It becomes nearly two times greater by the relation of nitrogen to oxygen charge equal to 0.8.

Now, assuming approximately $D \propto -\delta$, $E \propto -\epsilon$, some conclusions can be drawn. This is a rough approximation because of covalency, which was not taken into account in the point charge model, but when successfully tested for one complex, it can be successfully used for the second one. Because the calculated corresponding components of the electric-field gradient tensor are of comparable magnitude for both compounds, the values of D_i parameters for **NiBA** are expected to be comparable to those of **NiAA**. In turn, the values of rhombicity parameters are expected to be small ($D/E = \sim 10$ for terminal ions and $D/E = \sim 5$ for the central ions, as follows from the relations of corresponding δ and ϵ quantities in Table 4). During the fit, conditions $D_2 = D_3$ for the terminal ions and $E_i = 0$ for all ions were assumed. We were looking for the solution with $D_1 > 0$ (elongation)[10] and $D_2 = D_3 < 0$. There were together six parameters to fit. The best-fit parameters obtained for **NiAA** are given in Table 5. As seen, the signs of D_i values for **NiAA** agree with the signs of $-\delta_i$ in Table 4. Therefore, it was reasonable to use this method to find the solution for **NiBA**. The obtained parameters are given in Table 5. Fits obtained for both complexes are shown in Figures 4 and 5. The large value of $|D_{2,3}|$ for **NiBA** is at the limit of values reported for Ni(II) complexes.[10] It is responsible for the lower magnetization values of **NiBA** with respect to **NiAA** at 2 K (Figure 5). The obtained value of the TIP parameter, much larger than

(10) Boča, R. *Coord. Chem. Rev.* **2004**, *248*, 757.

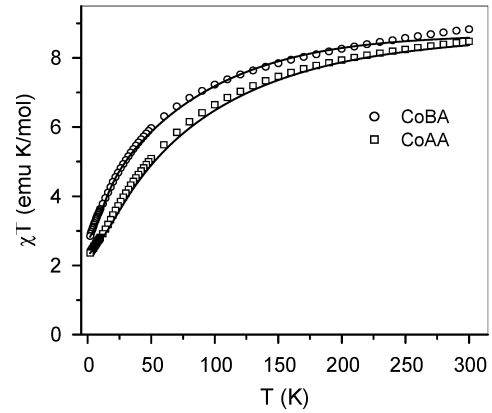

Figure 6. χT vs T for **CoAA** and **CoBA** complexes measured at H = 1000 Oe. Solid lines are fits (text).

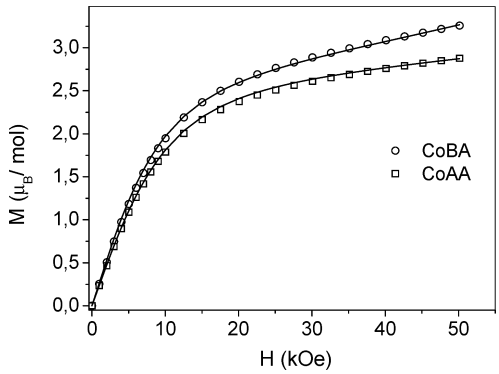

Figure 7. Magnetization vs field for **CoAA** and **CoBA** complexes measured at 2 K. Solid lines are fits (text).

for **NiAA**, is responsible for decreasing of the χT product with decreasing temperature in the high temperature range (Figure 4). The reason for the large TIP can be a small amount of some impurity. There is nearly no exchange coupling for the **NiBA** complex.

It should be noted that the solutions found for both complexes seem to be unique, as confirmed by fits of the equally good quality. This statement was also confirmed by Monte Carlo searches in the configurational parameter space. In the Supporting Information, exemplary $\chi T(T)$ and $M(H)$ curves are presented calculated for different sets of D and J parameters, thus demonstrating sensitivity of fit on changes of signs and values of these parameters.

4.2. Cobalt Trimers. Temperature dependence of the χT product and M versus H dependence (at 2 K) obtained for cobalt trimers are presented in Figures 6 and 7, respectively.

The Hamiltonian of the studied cobalt trimers includes spin−orbit coupling, low-symmetry crystal field term, magnetic exchange between cobalt ions, and Zeeman perturbation:

$$\hat{H} = \hat{H}_{SO} + \hat{H}_{Cr} + \hat{H}_{Ex} + \hat{H}_{Ze} \quad (4)$$

For each cobalt ion, the spin−orbit interaction within the $^4T_{1g}$ triplet can be written as:

$$\hat{H}_{SO} = -\frac{3}{2}\sum_i \kappa_i \lambda \hat{S}_i \cdot \hat{L}_i \quad (5)$$

where $\lambda = -170$ cm^{-1} is the spin−orbit coupling parameter

for the Co(II) ion and κ is the orbital reduction factor that takes into account both the covalency of the cobalt ligand bonds and the mixture of $^4T_{1g}$ states originated from ^4F and ^4P terms.[11]

The low-symmetry (noncubic) crystal field term takes into account the distortions of the local surroundings and, in general, can be written as:

$$\hat{H}_{Cr} = \sum_i \hat{L}_i \cdot \hat{\Delta}_i \cdot \hat{L}_i \quad (6)$$

where the $\hat{\Delta}_i$ tensor describes the splitting of the $^4T_{1g}$ term in the local crystal field. We suppose that in the local coordinate systems these tensors are diagonal for each of the cobalt ions and can be written in the similar way as the ZFS tensors for nickel ion (eq 2). In the molecular coordinate system, these tensors can be written as:

$$\hat{\Delta}_i = \nu_i^{-1} \hat{\Delta}_i^{loc} \nu_i \quad (7)$$

where orthogonal transformation matrices ν_i were described earlier.

The Zeeman interaction consists of both spin and orbital contribution and is

$$\hat{H}_{Ze} = \sum_i \mu_B H \cdot (g_0 \hat{S}_i - \frac{3}{2} \kappa_i \hat{L}_i) \quad (8)$$

where g_0 is the spin Lande factor.

As long as the ground-state of Co(II) is orbitally degenerate, the exchange interaction between cobalt ions should contain, in general, both orbital and spin contributions. Some ab initio calculations performed for the binuclear chlorine-bridged Co(II) complexes demonstrated that the energy pattern due to the exchange interaction can not be described by the simple Heisenberg scheme.[12] The exchange Hamiltonian deduced for the corner shared bioctahedral Co(II) of D_{4h} symmetry on the base of microscopic approach[13] demonstrates that the exchange interaction for this complex is essentially anisotropic. However in many cases the approach of Lines[14] that exchange between cobalt centers contains only an isotropic part operating with the real spins leads to reasonable explanation of the properties of corresponding complexes and the exchange part of the Hamiltonian can be written as the first term of eq 1.

We start the analysis of the cobalt trimers with the **CoAA** complex. Because of the symmetry of the system, it was assumed that $\kappa_2 = \kappa_3$ and $\Delta_2 = \Delta_3$, where Δ_i is the axial parameter of the $\hat{\Delta}_i^{loc}$ tensor. The powder averaged magnetic susceptibility can be calculated as $\chi_{av} = (\chi_x + \chi_y + \chi_z)/3$, whereas for the calculation of magnetization the averaging over all possible orientations of the external magnetic field should be performed. As distinguished from nickel trimers, in the case of cobalt complex this averaging procedure is time-consuming due to the large size of the matrices to be diagonalized (1728 × 1728 matrices) and some simplifications are required. The relatively strong spin−orbit coupling results in the ground doublet on each cobalt ion. This Kramers doublet is well separated from the excited levels. The effect of the low-symmetry crystal field does not change this conclusion (we neglect the case of very strong positive Δ, where the orbital angular momentum is completely quenched). As a result, at low temperatures only these ground Kramers doublets of each cobalt ion are thermally populated, and magnetization at $T = 2$ K can be well simulated with the use of perturbation theory.

Table 6. The Best Fit Parameters for Cobalt Trimers Obtained from Magnetic Data[a]

	CoAA	CoBA
Δ_1 (cm^{-1})	645 ± 5	372 ± 5
$\Delta_2 = \Delta_3$ (cm^{-1})	−642 ± 5	−775 ± 5
κ_1	0.92 ± 0.005	0.82 ± 0.005
$\kappa_2 = \kappa_3$	0.90 ± 0.005	0.88 ± 0.005
J_{ex} (cm^{-1})	−6.4 ± 0.05	−3.1 ± 0.05

[a] Uncertainties reflect the influence of the starting parameters and of the way of the minimization on the final results.

To obtain the key parameters of the studied complex the simultaneous fits of $\chi(T)$ and $M(H)$ were performed. The results are shown in Figures 6 and 7. The best fit parameters are given in Table 6.

The exchange interaction in the studied complex is found to be antiferromagnetic. The κ values are typical for this kind of complexes. The Δ_i parameters obtained in the best fit procedure are in agreement with the structural data. The ground state of the Co(II) ion in the octahedral surrounding represents a superposition of two $^4T_{1g}$ states, namely $|t_{2g}^5(^2T_{2g})e_g^2(^3A_2), {}^4T_{1g}\rangle$ and $|t_{2g}^4(^3T_{1g})e_g{}^3(^2E_g), {}^4T_{1g}\rangle$. The coefficients in this superposition depend on the strength of the crystal field; however, in any case the contribution of $t_{2g}^5e_g^2$ configuration is bigger. So, it can be assumed that the behavior of the high-spin Co(II) ion with symmetry lowering is determined by the behavior of this electronic configuration. The axial distortion along local z axis leads to the splitting of e_g and t_{2g} states. The compression leads to the stabilization of d_{xy} orbital, whereas for elongation d_{xz} and d_{yz} are the lowest in energy. The obtained states can be filled in with 7 d-electrons, and one finds that for $t_{2g}^5e_g^2$ configuration the compression results in the doubly degenerate ground-state, whereas for the elongation there is no orbital degeneracy. In terms of eq 6, it means that the compression and the elongation of the local surrounding can be described with the negative and positive values of Δ_i parameters, respectively. So, the positive value of Δ_1 and negative values of $\Delta_2 = \Delta_3$ parameters agree with the conclusions about distortions around the central and terminal ions made on the analysis of the crystal-field gradient tensor (part 4.1).

The experimental MCD spectra of CoAA are presented in Figure 8. They are dominated by temperature-dependent contributions. The strong signal at 324 nm corresponds to the metal−ligand charge transfer, whereas bands at 495 and 510 nm are typical for d−d transitions. To construct the saturation magnetization curves, we recorded signal intensities at the maxima of all three bands for temperatures up to 7 K. The results are shown in Figure 9. There are two different types of behavior. The signal at 324 nm is

(11) Kahn, O. *Molecular Magnetism*; VCH Publishers: New York, 1993.
(12) Fink, K.; Wang, C.; Staemmler, V. *Inorg. Chem.* **1999**, *38*, 3847.
(13) Palii, A. V.; Tsukerblat, B. S.; Coronado, E.; Clemente-Juan, J. M.; Borras-Almenar, J. J. *J. Chem. Phys.* **2003**, *118*, 5566.
(14) Lines; M.E., *J. Chem. Phys.* **1971**, *55*, 2977.

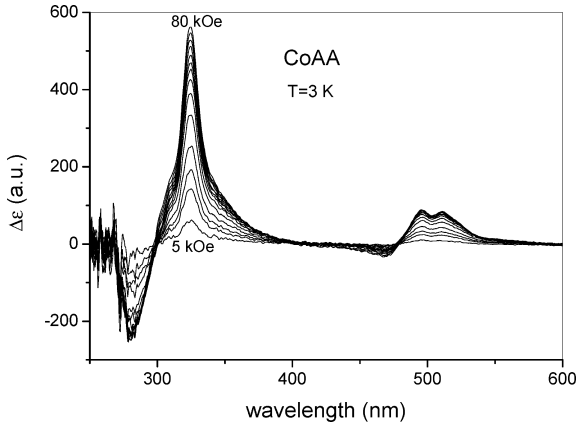

Figure 8. Experimental MCD spectrum of **CoAA** recorded at 3 K by fields up to 80 kOe.

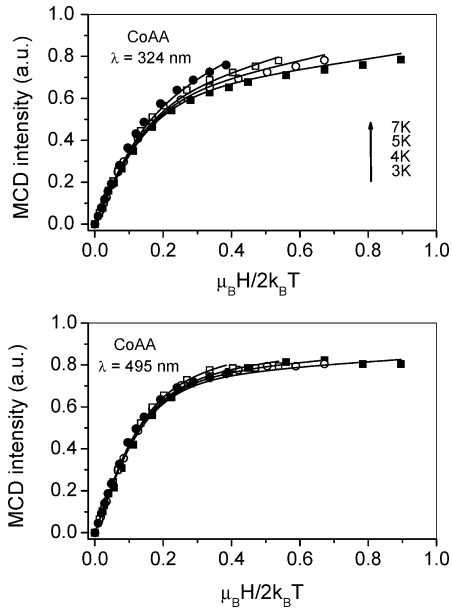

Figure 9. Comparison of calculated and measured magnetization curves for the **CoAA** complex at 324 nm (top, calculations were done at the assumptions $M_{xy} = 0$, $M_{xz} = M_{yz}$) and 495 nm (bottom, calculations were done at the assumptions $M_{xz} = M_{yz} = 0$).

temperature dependent, whereas for 495 and 510 nm saturation curves recorded at different temperatures practically coincide. The different behavior of the signal at different wavelength is typical for the complexes where orbital angular momentum is partially or completely quenched[15–17] and can be regarded as a confirmation of the relatively large values of low-symmetry crystal-field parameters obtained earlier.

The magnetization curves in Figure 9 look similar to those from the magnetic measurements presented in Figure 7. However, the temperature and field dependence is different because MCD signal depends both on the ground and excited states and, as a consequence, on the polarization of the corresponding optical transitions. Even if this polarization is unknown from the experiment, MCD curves provide some additional information and allow one to determine the key parameters of the system more accurate.

In the case of mononuclear complexes with the orbitally degenerate ground-state, MCD saturation behavior depends on the polarization of the corresponding transitions and can be simulated with the use of eq 9: [17]

$$\Delta\varepsilon(\vartheta,\phi) \propto M_{xy}\cos\vartheta\langle L^z\rangle_T + M_{xz}\sin\vartheta\sin\phi\langle L^y\rangle_T + M_{yz}\sin\vartheta\cos\phi\langle L^x\rangle_T \quad (9)$$

where $\langle L^k\rangle_T$ is thermally and orientationally averaged component of the orbital angular momentum within the ground state:

$$\langle L^k\rangle_T = \frac{1}{Z}\sum_g \langle g|L^k|g\rangle \exp(-E_g/k_BT),\ k = x,\ y,\ z \quad (10)$$

where Z is a partition function, and ϑ and ϕ describe the orientation of the magnetic field with respect to the molecule-fixed coordinate system. To obtain the signal from the randomly oriented molecules in frozen Nujol, eq 9 is integrated over all magnetic field orientations.

To check if these equations are also applicable to the case of complexes of exchange coupled ions with orbitally degenerate ground states, we use them for simulation of MCD behavior of the **CoAA** trimer. The result is shown in Figure 9. The theoretical curves are calculated at the assumption $M_{xz} = M_{yz} = 0$ ($\lambda = 495$ nm) and $M_{xy} = 0$, $M_{xz} = M_{yz}$ ($\lambda = 324$ nm). There is reasonable agreement between the experimental data and theoretical curves. This agreement confirms the applicability of the model to the theoretical explanation of the magneto-optical behavior of the investigated cobalt trimer. Small differences between the theory and experiment can be caused by the fact that the Lines approach neglects the anisotropy of the exchange interaction. However, this anisotropy could play a role at low temperatures.

At the next stage of investigations, the model presented above was applied to the explanation of behavior of the **CoBA** complex. The experimental $\chi T(T)$ and $M(H)$ dependences, as well as theoretical fits are presented in Figures 6 and 7. The best-fit parameters are given in Table 6. One can see that for both complexes the obtained single ion parameters are similar. The only essential difference is in the magnitude of the exchange interaction. In the **CoAA** complex, this interaction is stronger due to the shorter distances between metal ions and bridging oxygen. Like for **CoAA** complex, the experimental MCD spectrum of the **CoBA** trimer consists of three bands located at 324, 495, and 510 nm. As distinguished from the previous case, now the saturation curves are temperature dependent not only for the metal−ligand charge transfer (324 nm) but for the d−d transitions (495 and 510 nm) as well (compare Figures 9, 10). Nevertheless, the signal behavior at 495 and 510 nm can be well reproduced at the assumption of *xy* polarization of the corresponding transitions just like as in the **CoAA** system. As for the magnetization curves at 324 nm, the computer simulation with the use of eqs 9 and 10 demonstrates that the transitions of all polarizations contribute to this MCD signal.

(15) Ostrovsky, S. M.; Falk, K.; Pelikan, J.; Brown, D. A.; Tomkowicz, Z.; Haase, W. *Inorg. Chem.* **2006**, *45*, 688.
(16) Neese, F.; Solomon, E. I. *Inorg. Chem.* **1999**, *38*, 1847.
(17) Oganesyan, V. S.; George, S. J.; Cheesman, M. R.; Thomson, A. J. *J. Chem. Phys.* **1999**, *110*, 762.

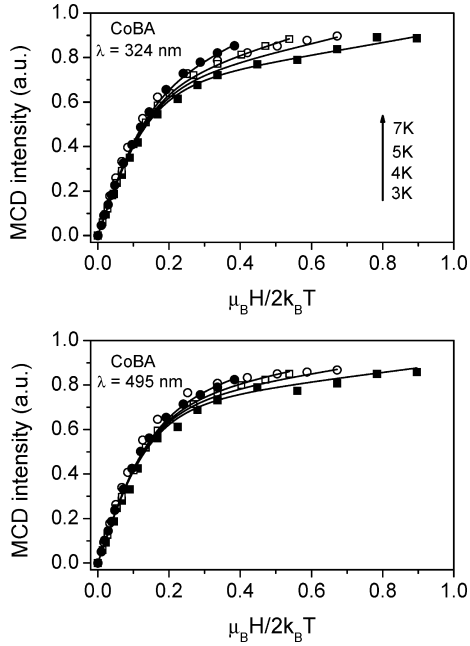

Figure 10. Comparison of calculated and measured magnetization curves for **CoBA** at 324 nm (top, calculations were done at the assumptions $M_{xy} = 3M_{xz} = 3M_{yz}$) and 495 nm (bottom, calculations were done at the assumptions $M_{xz} = M_{yz} = 0$).

5. Discussion

Three new trinuclear complexes $[Ni_3(\mu\text{-}OAc_F)_4(\mu\text{-}AA)_2(tmen)_2]$, $[Ni_3(\mu\text{-}OAc_F)_4(\mu\text{-}BA)_2(tmen)_2]$, and $[Co_3(\mu\text{-}OAc_F)_4(\mu\text{-}BA)_2(tmen)_2]$ have been synthesized and their crystal structures were determined. These complexes and the related $[Co_3(\mu\text{-}OAc_F)_4(\mu\text{-}AA)_2(tmen)_2]$ were magnetically characterized.

Metal ions in all studied compounds have distorted octahedral coordination. The central M ion has coordination O_6. The terminal M ions are in the N_2O_4 coordination environment. Each pair of the nearest neighbors M ions is triply bridged by one hydroxamate bridge and two trifluoroacetate bridges. The dominating magnetic exchange is through M−O−M path of the hydroxamate bridge (superexchange through one intermediary).

For the nickel case, the sign of the exchange integral J_{ex} depends on the Ni−O−Ni angle. The linear relationship was found between the value of J_{ex} and this bridging angle, for which a limit value of 97° is anticipated[18] for the transition from ferromagnetic (angle < 97°) to antiferromagnetic coupling. There are known some dinuclear, related to urease, nickel complexes with Ni−O−Ni bonding angle below 97 and they have ferromagnetic Ni−Ni coupling.[19–21] There were also reported (μ-oxo)bis(μ-carboxylato) dinuclear nickel complexes[22–26] with a Ni−O−Ni bonding angle above 97°, that is, in the range 111.9−118.0°. They all have antiferromagnetic coupling with J_{ex} values in the range −1.9 to –3.5 cm^{-1}. There exist, however, (μ-oxo)bis(μ-carboxylato) dinuclear nickel complexes with Ni−O−Ni angle greater than 97° and ferromagnetic coupling. We can quote one case,[27] where the Ni−O−Ni angle is 113.6° and J_{ex}= +2 cm^{-1}. The complex **NiAA**, studied in the present work, is a new complex with ferromagnetic Ni−Ni coupling by a relatively large Ni−O−Ni angle equal to 117°. The essential difference with respect to the case of ref 27 is that the methyl group of the acetate group is substituted by CF_3. One can conclude that the acetate bridge contributes ferromagnetic coupling and that the coupling through the trifluoro-acetate bridge is stronger than through the acetate bridge.

In **NiBA**, there is nearly no coupling, likely because of compensation of the three bridges contributions. The large value of *D* parameter, obtained for this complex, is near the limit of highest values reported for the Ni(II) ion in a distorted octahedral surrounding.[9] This can be caused by the aromatic ring attached to the hydroxamate bond.

Both cobalt trimers are explained in the same model with similar single ion parameters. The difference in the magneto-optical behavior of these systems is mainly caused by the magnitude of the magnetic exchange between Co(II) ions. For comparison, some isolated dimeric and trimeric Co(II) complexes were magnetically studied recently,[28–30] and in all complexes the exchange interaction was antiferromagnetic. The typical value of this exchange for water-bridged complexes is about –0.5 to –0.7 cm^{-1}, whereas for hydroxamate bridged ones the value of this interaction reaches several wave numbers (for example, in the $[Co_2(\mu\text{-}OAc)_2(\mu\text{-}AA)(urea)(tmen)_2]$ dimer $J_{ex} = -3.6$ cm^{-1}). In the present work, we obtained the similar values of the magnetic exchange for acetohydroxamate and benzohydroxamate bridged compounds. It should be mentioned once again that in general this exchange could be anisotropic. However, the approach of Lines[14] used in our investigations gives a good explanation of the experimental results.

Acknowledgment. Z.T., W.H., and S.O. thank DFG for the financial support.

Supporting Information Available: Listings of crystallographic data in CIF format. Derivation of ν_i matrices. Two figures demonstrating sensitivity of the calculated χT and magnetization curves to the signs of *D* and to the value of *J* parameters. This material is available free of charge via the Internet at http://pubs.acs.org.
IC800264Y

(18) Nanda, K. K.; Thompson, L. K.; Bridson, J. N.; Nag, K. J. *J. Chem. Soc., Chem. Commun.* **1994**, 1337.
(19) Arnold, M.; Brown, D. A.; Deeg, O.; Errington, W.; Haase, W.; Herlihy, K.; Kemp, T. J.; Nimir, H.; Werner, R. *Inorg. Chem.* **1998**, *46*, 2920.
(20) Paital, A. R.; Wong, W. T.; Aromi, G.; Ray, D. *Inorg. Chem.* **2007**, *46*, 5727.
(21) Brown, D. A.; Glass, W. K.; Fitzpatrick, N. J.; Kemp, T. J.; Errington, W.; Clarkson, G. J.; Haase, W.; Falk, K.; Mahdy, A. H. *Inorg. Chim. Acta* **2004**, *357*, 1411.
(22) Volkmer, D.; Hörstmann, A.; Griesar, K.; Haase, W.; Krebs, B. *Inorg. Chem.* **1996**, *35*, 35.
(23) Buchanan, R. M.; Mashuta, M. S.; Oberhausen, K. J.; Richardson, J. F. *J. Am. Chem. Soc.* **1989**, *111*, 4497.
(24) Greatti, A.; de Brito, M. A.; Bortoluzzi, A. J.; Ceccato, A. S. *J. Mol. Struct.* **2004**, *688*, 185.
(25) Adams, H.; Bradshaw, D.; Fenton, D. E. *Inorg. Chim. Acta* **2002**, *332*, 195.
(26) Greatti, A.; Scarpellini, M.; Peralta, R. A.; Casselato, A.; Bortoluzzi, A. J.; de Brito, M. A.; Szpoganicz, B.; Tomkowicz, Z.; Haase, W.; Neves, A. *Inorg. Chem.* **2008**, *47*, 1107.
(27) Eremenko, I. L.; Nefedow, S. E.; Sidorov, A. A.; Golubnichaya, M. A.; Danilov, P. V.; Ikorskii, V. N.; Shvedenkov, Y. G.; Novotortsev, V. M.; Moiseev, I. I. *Inorg. Chem.* **1999**, *38*, 3764.
(28) Calvo-Perez, V.; Ostrovsky, S.; Vega, A.; Pelikan, J.; Spodine, E.; Haase, W. *Inorg. Chem.* **2006**, *45*, 644.
(29) Brown, D. A.; Errington, W.; Glass, W. K.; Haase, W.; Kemp, T. J.; Nimir, H.; Ostrovsky, S. M.; Werner, R. *Inorg. Chem.* **2001**, *40*, 5962.
(30) Ostrovsky, S. M.; Werner, R.; Brown, D. A.; Haase, W. *Chem. Phys. Lett.* **2002**, *353*, 290.